Science Bulletin 66 (2021) 62–68

Contents lists available at ScienceDirect

Science Bulletin

journal homepage: www.elsevier.com/locate/scib

Article

Controllable CO adsorption determines ethylene and methane productions from CO_2 electroreduction

Haipeng Bai [a], Tao Cheng [b], Shangyu Li [a], Zhenyu Zhou [a], Hao Yang [b], Jun Li [c], Miao Xie [b], Jinyu Ye [d], Yujin Ji [b], Youyong Li [b], Zhiyou Zhou [d], Shigang Sun [d], Bo Zhang [a,*], Huisheng Peng [a,*]

[a] State Key Laboratory of Molecular Engineering of Polymers, Department of Macromolecular Science and Laboratory of Advanced Materials, Fudan University, Shanghai 200438, China
[b] Institute of Functional Nano & Soft Materials (FUNSOM) and Jiangsu Key Laboratory for Carbon-Based Functional Materials & Devices, Soochow University, Suzhou 215123, China
[c] Institute of Chemical Sciences and Engineering, École polytechnique fédérale de Lausanne, Lausanne 1015, Switzerland
[d] State Key Laboratory of Physical Chemistry of Solid Surfaces, Collaborative Innovation Center of Chemistry for Energy Materials, College of Chemistry and Chemical Engineering, Xiamen University, Xiamen 361005, China

ARTICLE INFO

Article history:
Received 11 April 2020
Received in revised form 22 April 2020
Accepted 22 April 2020
Available online 16 June 2020

Keywords:
CO_2 electroreduction
CO adsorption
Hydrogenation
Dimerization

ABSTRACT

Among all CO_2 electroreduction products, methane (CH_4) and ethylene (C_2H_4) are two typical and valuable hydrocarbon products which are formed in two different pathways: hydrogenation and dimerization reactions of the same CO intermediate. Theoretical studies show that the adsorption configurations of CO intermediate determine the reaction pathways towards CH_4/C_2H_4. However, it is challenging to experimentally control the CO adsorption configurations at the catalyst surface, and thus the hydrocarbon selectivity is still limited. Herein, we seek to synthesize two well-defined copper nanocatalysts with controllable surface structures. The two model catalysts exhibit a high hydrocarbon selectivity toward either CH_4 (83%) or C_2H_4 (93%) under identical reduction conditions. Scanning transmission electron microscopy and X-ray absorption spectroscopy characterizations reveal the low-coordination Cu^0 sites and local Cu^0/Cu^+ sites of the two catalysts, respectively. CO-temperature programed desorption, *in-situ* attenuated total reflection Fourier transform infrared spectroscopy and density functional theory studies unveil that the bridge-adsorbed CO (CO_B) on the low-coordination Cu^0 sites is apt to be hydrogenated to CH_4, whereas the bridge-adsorbed CO plus linear-adsorbed CO (CO_B + CO_L) on the local Cu^0/Cu^+ sites are apt to be coupled to C_2H_4. Our findings pave a new way to design catalysts with controllable CO adsorption configurations for high hydrocarbon product selectivity.

1. Introduction

CO_2 electroreduction (CO_2RR), powdered by renewable electricity, provides a promising way to reduce greenhouse gas net emission, store the intermittent renewable clean energy and generate industrial feedstock [1,2]. Up to now, only copper (Cu) catalysts can give a rich gamut of single-carbon and multi-carbon products [3,4]. However, the reduction pathways often furcate to form a wide range of products, which are affected by both the chemical properties of catalysts and reduction reaction conditions [5].

Among all reduction products, only a few primary products like CO and HCOOH can be achieved with a high selectivity (i.e., Faradic efficiency (FE)) of >95% [6,7]. The production of either CO or HCOOH is related to a two-electron process, typically starting from relative fixed CO_2 adsorption configurations [8]. For instance, the C-bonded CO_2 adsorption configurations on Au, Ag, Pd surfaces [9–11] undergo a proton-coupled electron transfer process to *COOH for CO formation, whereas O-bonded CO_2 adsorptions on Bi, Sn and Pb surfaces [6,12] transform to *OCHO for HCOOH production. The simple production pathways with controlled CO_2 adsorption configurations lead to the high selectivity of CO or HCOOH.

In contrast, the hydrocarbon products are derived from the *CO intermediate and subsequent more complicated reaction pathways [9,13], but *CO absorption configurations on the Cu catalysts are not well controllable, so the hydrocarbon product selectivity is not as high as the selectivity of CO or HCOOH. The reduction of *CO intermediate mainly results in C_1 productions such as CH_4 via a hydrogenation pathway and C_2 productions such as C_2H_4 via a dimerization pathway [14]. Theoretical studies have shown that different *CO configurations and adsorption energies on the

* Corresponding authors.
E-mail addresses: bozhang@fudan.edu.cn (B. Zhang), penghs@fudan.edu.cn (H. Peng).

https://doi.org/10.1016/j.scib.2020.06.023

Cu catalysts [15,16] can result in different energy barriers of CO hydrogenation or dimerization reactions [17–19].

The CO adsorption configuration and adsorption energy rely on a number of factors, such as the surface structures of catalysts which can be affected by composition [20], particle size [21], grain boundary [22], facet [23] and so on, and reduction reaction conditions of applied potentials [24], electrolyte species [25], local pH [26], electrolyte concentration [27], etc. For instance, a low-coordination Cu is potential to facilitate the translation of *CO to *CHO, and thus facilitate the C_1 pathway [23,28]. By contrast, the coupling reaction of *CO is highly related to the local valence structure of Cu in which the local Cu^0/Cu^+ site is reported to promote the dimerization and therefore enhance the C_2 production [20,29].

It is still challenging to control the variate that affects the *CO absorption configurations on Cu experimentally, thus it remains difficult to modulate the reaction pathways and final products [21,30]. Especially, the formations of CH_4 and C_2H_4 are always concomitant on the Cu catalysts when the reaction parameters are similar, which makes it even more difficult to distinguish the contributions of *CO adsorption properties. It is therefore necessary to obtain well-defined model catalysts with controllable *CO absorption configurations that can catalyze CO_2 towards highly selective CH_4 and C_2H_4 productions in identical reduction conditions.

Herein, using a controlled variation method, we develop two catalysts with controlled and distinct active sites. The low-coordination Cu catalysts show a high CH_4 selectivity of 83% while the Cu/Cu_2O catalysts exhibit a high C_2H_4 selectivity of 93% under identical reduction conditions. We study the CO adsorption properties and establish a correlation between the CO adsorption and reduction pathways on these two model catalysts, with the aid of CO temperature-programed desorption (TPD), *in-situ* attenuated total reflection Fourier transform infrared spectroscopy (ATR-FTIR) and density functional theory calculations. These results show that the bridge-adsorbed CO (CO_B) on the low-coordination Cu^0 site is apt to be hydrogenated to form CH_4, whereas the bridge-adsorbed CO plus linear-adsorbed CO (CO_B + CO_L) on the local Cu^0/Cu^+ site is apt to be coupled to form C_2H_4.

2. Experimental

The two catalysts were prepared via an epoxide-assisted hydrolysis method and were activated during CO_2RR. The chemical structures of the catalysts were studied by scanning transmission electron microscopy (STEM) and X-ray absorption spectroscopy (XAS). The CO adsorption properties were studied by TPD and ATR-FTIR. The details of the preparation and characterization can be found in Supplementary materials (online).

3. Results and discussion

3.1. Structures characterizations

Inspired by the chemical structure modulating capability of halogens on the Cu catalyst [31,32], we sought to introduce halogen modifiers into the catalyst precursors to construct different Cu catalysts with either low-coordination or local Cu^0/Cu^+ sites. Experimentally, we successfully synthesized two Cu catalysts derived from bromine-doped (Figs. S1–S3 online) and iodine-doped copper oxychlorides (Figs. S4–S6 online), respectively [7,33] (see Supplementary materials (online) for details): one contains a low-coordination Cu^0 phase for potentially high CH_4 selectivity, denoted as methane production copper (MP-Cu); the other possesses Cu^0/Cu^+ sites for potentially high C_2H_4 selectivity,

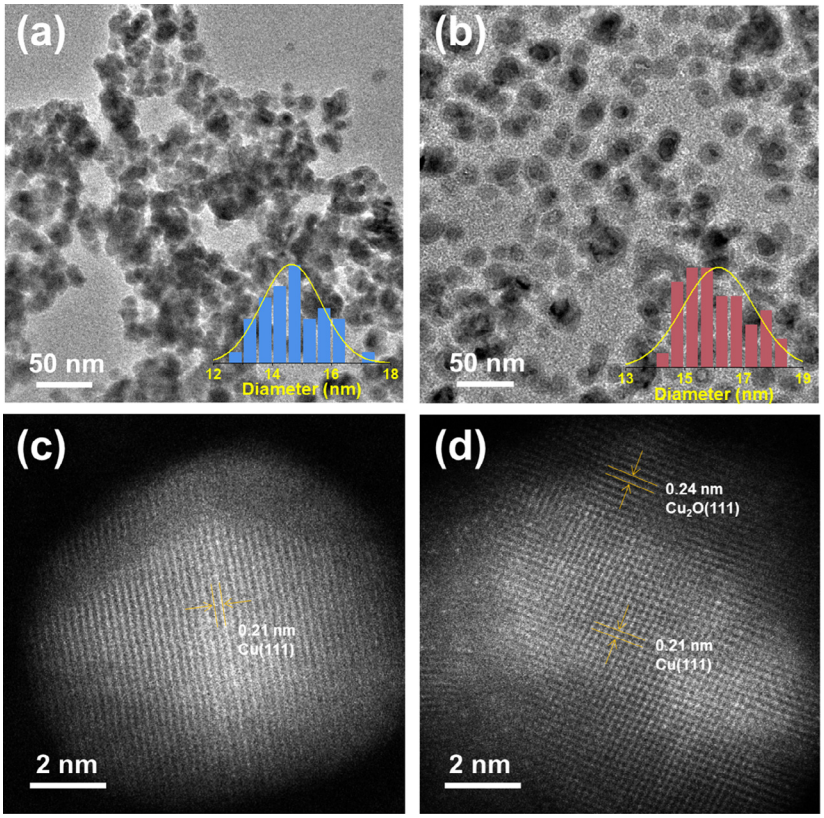

Fig. 1. (Color online) Morphology characterizations. (a), (b) TEM images of the MP-Cu and EP-Cu catalysts. Insets show a uniform particle size of ~15 nm for both catalysts. (c), (d) STEM images of a representative catalyst particle of EP-Cu and MP-Cu, revealing the Cu^0 phase with abundant step sites in MP-Cu while abundant local Cu^0/Cu^+ sites in EP-Cu.

denoted as ethylene production copper (EP-Cu). The two catalysts were activated using *in-situ* electrochemical reduction processes. No halogen residual was presented in the activated catalysts as shown in the X-ray photoelectron spectroscopy (XPS) and energy dispersive spectroscopy (EDS) results (Figs. S7 and S8 online).

To study the structures of the catalysts, we firstly carried out morphology characterizations. Fig. 1a and b represent the transmission electron microscopy (TEM) images of the two catalysts. Both MP-Cu and EP-Cu are nano-sized particles with ~15 nm diameter (Figs. S9 and S10 online), from which we excluded the influences of catalyst particle size on the reduction performance. High-resolution STEM images show distinct crystal structures of the two catalysts. The MP-Cu shows only one Cu^0 phase with surface step sites (Fig. 2c) while EP-Cu shows two phases containing both Cu^0 and Cu^+, indicating the abundant local Cu/Cu^+ sites (Fig. 2d). Taken the TEM results together, we preliminarily conclude that the two catalysts were synthesized as designed.

To study the electronic structures of the two catalysts, we performed the Cu K-edge XAS measurements (see Supplementary materials (online) for details). By comparing the absorption thresholds of the X-ray absorption near edge structure (XANES), we extracted the valence states of the catalysts [33,34] (Fig. S11 online). The absorption threshold of MP-Cu shifts from Cu^{2+} (8985.1 eV) to Cu^0 (8979.0 eV) and becomes stable (Fig. 2a) after a 30-min reduction process, indicating MP-Cu almost contains only Cu^0 species. The linear combination fit results of XANES of MP-Cu confirm the metallic Cu nature during CO_2RR (Fig. 2b, see Supporting materials (online) for details). Extended X-ray absorption fine structure (EXAFS) of MP-Cu at the Cu K-edge reveals that the sample contains almost no Cu–O path but dominant Cu-Cu path (R = 2.54 Å). MP-Cu shows a low Cu-Cu coordination number of ~7, which is much lower than that of Cu foil (with a Cu-Cu coordination number of ~12), indicating a potential of MP-Cu towards highly selective CH_4 production from CO_2RR (Fig. S12a, Table S1 online) [21,28]. For EP-Cu, the absorption threshold is stabilized at 8979.4 eV, revealing an intermediate valence between Cu^+ (8980.3 eV) and Cu^0 (Fig. 2c). The linear combination fit results of XANES of EP-Cu at the Cu K-edge suggest that EP-Cu contains 47% of Cu^0 and 53% of Cu^+ (Fig. 2d). The Cu K-edge EXAFS of EP-Cu shows an intense Cu–O path (R = 1.85 Å) similar to that of Cu_2O [35] (Fig. S12b online), which further confirms the Cu/Cu^+ structure that is supposed to be active in C_2H_4 production [20,29]. Both morphology and XAS studies show that the two catalysts have similar particle size but controllable surface chemical structures, and therefore can work as model catalysts for hydrocarbon production.

3.2. CO_2 electroreduction performance

We then evaluated the CO_2 reduction performances of the two catalysts. CO_2RR tests were carried out using 0.05 mol L^{-1} $KHCO_3$ aqueous solution as electrolytes. All reduction conditions were controlled to eliminate the undesired influences of experimental variables (Table S2 online). Fig. 3 represents the CO_2RR results of the MP-Cu and EP-Cu catalysts. The two catalysts show distinct selectivities towards CH_4 and C_2H_4, respectively. The MP-Cu shows 59% ± 1% CH_4 FE at −1.71 V versus reversible hydrogen electrode (vs. RHE) (Figs. 3a and S13a online). The corresponding carbon selectivity of CH_4 comparing to all carbon-containing products reaches up to 83% (Fig. 3b and Fig. S13b online). In contrast, the

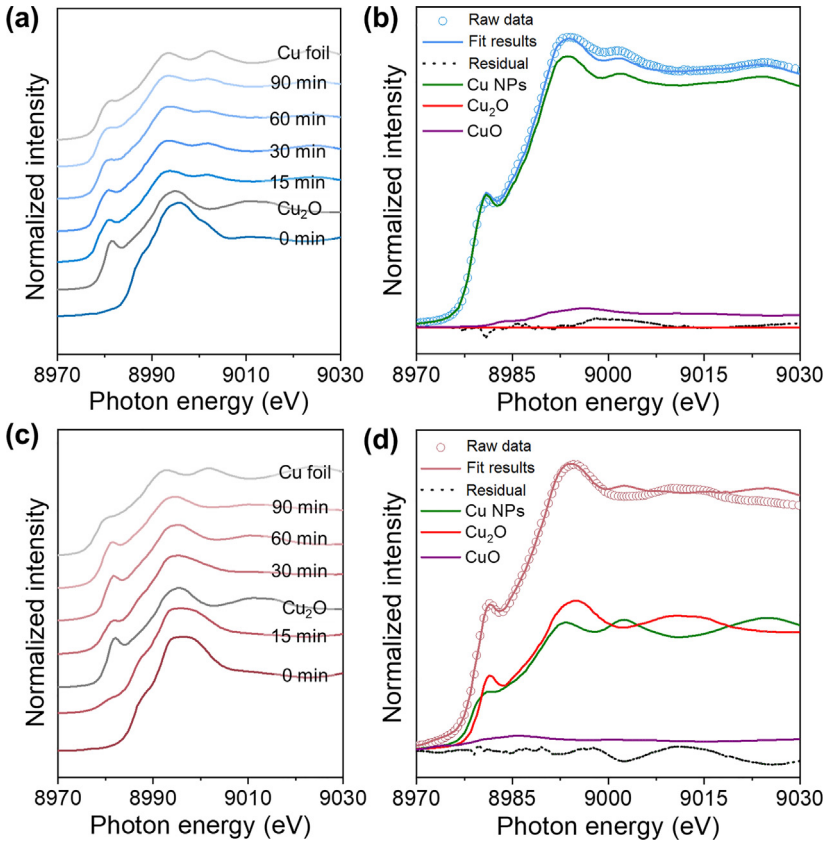

Fig. 2. (Color online) XAS characterizations of the MP-Cu and EP-Cu. (a) Cu K-edge XANES spectra of MP-Cu versus time, showing the valence states of Cu from initial 2+ to the stabilized 0. (b) Linear combination fit results of MP-Cu XANES at the Cu K-edge acquired in 90 min using Cu, Cu_2O and CuO NPs as standards (fitting range: 8970–9030 eV). (c) Cu K-edge XANES spectra of EP-Cu versus time, showing the valence states of Cu from initial 2+ to the stabilized positively charged Cu. (d) Linear combination fit results of EP-Cu XANES at the Cu K-edge acquired in 90 min using Cu, Cu_2O and CuO NPs as standards (fitting range: 8970–9030 eV).

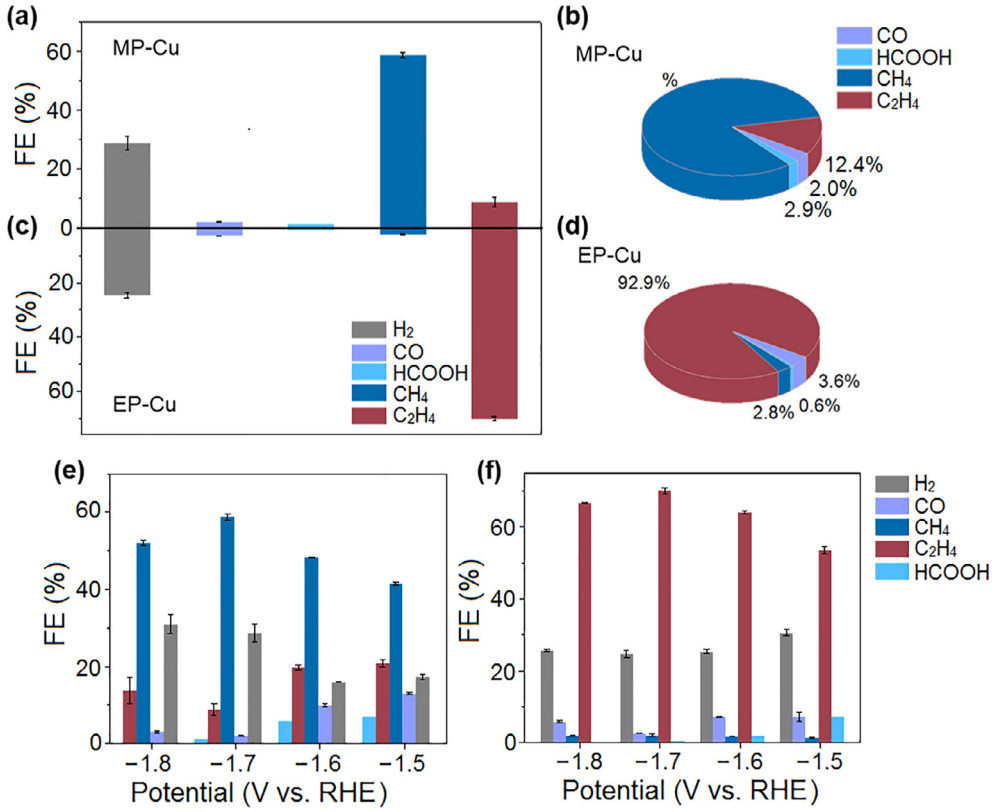

Fig. 3. (Color online) CO_2RR performance of MP-Cu and EP-Cu. (a) FE distribution of reduction products on MP-Cu and (b) carbon selectivity distribution comparing to all carbon containing products of MP-Cu at optimized potential. (c) FE distribution of reduction products on MP-Cu and (d) carbon selectivity distribution comparing to all carbon containing products of MP-Cu at optimized potential. (e) FE distribution of reduction products on MP-Cu versus applied potential. (f) FE distribution of reduction products on EP-Cu versus applied potential.

commercial Cu without the low-coordination site show a much lower CH_4 selectivity under the same CO_2 reduction conditions, suggesting the intrinsic high CH_4 selectivity of MP-Cu (Fig. S14 online). At the same applied potential, the FE and carbon selectivity of C_2H_4 produced on EP-Cu are 70% ± 1% and 93%, respectively (Fig. 3c and d). Furthermore, Fig. 3e, f and Figs. S15, S16 (online) represent the CH_4 and C_2H_4 FEs of MP-Cu and EP-Cu at various applied potentials. Under all applied potentials, MP-Cu shows a high CH_4 selectivity while EP-Cu shows a high C_2H_4 selectivity. Thus, we conclude that the MP-Cu and EP-Cu catalysts have intrinsic high selectivities towards CH_4 and C_2H_4, respectively, compared to previously reported catalysts (Fig. S17 online). The two catalysts also present robust stabilities without an obvious FE decrease after running CO_2RR for 9000 s (Fig. S18 online). The local pH is a parameter that may cause differences in selectivity and it mainly depends on the electrode geometry, electrolyte, and current density [26,36]. In this study, the electrode geometry and electrolyte are identical in the two reduction processes. As a result, the difference in local pH mainly comes from the applied current density. To study the influence of local pH, we further measured the cyclic voltammetry curves of the two catalysts (Figs. S19–S21 online). The results show similar current densities of the two catalysts under the same applied potential, excluding the contribution of local pH on the reduction pathways in this study.

3.3. CO adsorption study

To bridge the catalytic structures and CO_2 reduction performance, the CO adsorption properties of the two catalysts were studied. Generally, the adsorbed CO differs in adsorption configurations (linear, bridge, and multi adsorption) and in adsorption energy [37,38]. The adsorption energy of bridge-adsorbed CO (CO_B) is stronger than that of linear-adsorbed CO (CO_L) but weaker than that of multi-adsorbed CO (CO_M). We firstly used CO-TPD to evaluate the adsorption strength of CO on different catalysts. As shown in the TCD results, at a temperature range lower than 550 ℃, MP-Cu shows only one obvious desorption peak at 481 ℃ that can be attributed to CO_B, while EP-Cu shows two desorption peaks at 453 and 218 ℃ that can be attributed to CO_B and CO_L, respectively (Fig. 4a) [39,40]. The peaks at temperature exceeding 550 ℃ can be ascribed to CO_M that is firmly bonded on the catalyst (Fig. S22 online) and presumably inactive during the reduction process [41,42].

Furthermore, surface sensitive *in-situ* ATR-FTIR spectroscopy was applied to study the surface adsorbed CO under different applied potentials. It is apparent that both MP-Cu and EP-Cu show an adsorption peak at ~1900 cm^{-1} in associated with CO_B, while EP-Cu shows an additional adsorption peak at ~2080 cm^{-1} attributable to the weakly adsorbed CO_L (Fig. 4b and c) [38,42,43]. From the CO adsorption studies, both CO-TPD and *in-situ* ATR-FTIR results suggest the consistent conclusion that there is only one CO adsorption configuration on MP-Cu (CO_B) while there are two CO adsorption configurations on EP-Cu (both CO_B and CO_L).

To further study the relationship between the Cu oxidation state and CO adsorption, we further carried out CO-TPD measurements of commercial Cu and Cu_2O NPs as controls. As shown in Fig. S23 (online), each sample shows only one dominate desorption peak, i.e., 210 ℃ (CO_B) for Cu_2O NPs and 430 ℃ (CO_L) for Cu NPs before 550 ℃ (see Supplementary materials (online) for details). It can be seen from the CO-TPD results that the CO_B adsorption energy of MP-Cu is stronger than that of Cu NPs, which can be ascribed to its lower Cu-Cu coordination numbers. Taken together

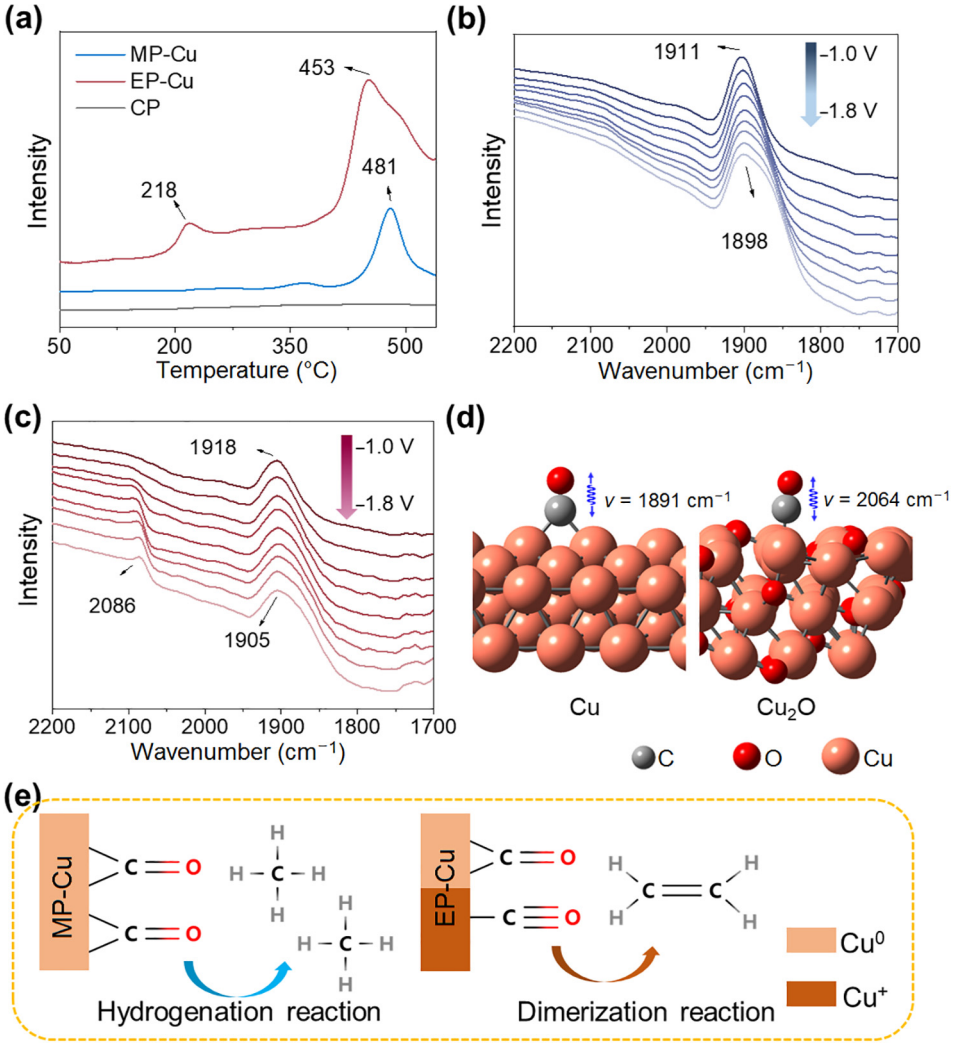

Fig. 4. (Color online) CO adsorption studies of EP-Cu and MP-Cu. (a) CO TPD results of EP-Cu, MP-Cu and the catalysts support carbon paper (CP), showing only CO_B on MP-Cu while both CO_L and CO_B on EP-Cu. (b) *In-situ* ATR-FTIR study of MP-Cu versus applied potential, representing only CO_B on MP-Cu. (c) *In-situ* ATR-FTIR study of EP-Cu versus applied potential, revealing both CO_L and CO_B on EP-Cu. (d) Optimized CO adsorption configuration and relative vibration frequency on step site (bridge, left side) and on oxidized site (linear, right side) after removing the beneath Cu to show the sub-surface oxygen from DFT results (side views). (e) Illustration of different CO adsorption configurations towards either hydrogenation or dimerization reaction pathways.

with previous structure results, it can be concluded that MP-Cu containing only a low-coordination Cu^0 phase shows only CO_B in accordance with commercial Cu NPs, and EP-Cu containing both Cu^0 phase and Cu^+ phases possess both CO_B and CO_L and the peak positions are adjacent to relative desorption peaks of Cu NPs and Cu_2O NPs. Thus, we experimentally conclude that CO is apt to adsorb on the Cu^0 sites with a strong bridge configuration while on the Cu^+ sites with a weak linear configuration.

To further understand our experimental results, we carried out DFT calculations with generalized gradient approximations (GGA) of Perdew-Burke-Ernzerhof (PBE) functional to investigate the CO adsorption property and possible active sites on MP-Cu and EP-Cu. As indicated from the CO adsorption results, only strong CO_B binding sites exist on MP-Cu. The strong binding sites, other than rhombi sites or square sites from basal planes, are likely step sites (low-coordination sites) as shown in Figs. 1c, 4d and Fig. S24a (online). We, therefore, carried out DFT calculations to verify the vibration frequency of CO on this step site, which leads to a prediction of 1891 cm^{-1}, very close to the experimental observations of 1898 to 1911 cm^{-1}. In our previous work, we determined that this step site can greatly reduce the formation energy of *CHO [44] from the reduction of *CO intermediate, the first step of CO hydrogenation, which is known as both the potential determining step or rate determining step in the pathway of CH_4 formation. Thus, the presence of step site can greatly catalyze the formation of CH_4, which explains the highly selective CH_4 production as observed experimentally.

In our previous work, we found that partially reduced Cu_2O generates Cu sites carrying partial charges ($Cu^{\delta+}$), which can provide a fairly strong linear CO binding site for the further CO coupling reaction [45]. The atomic structure of one of the representative sites is shown in Fig. 4d and Fig. S24b (online). From DFT calculations, we found the C–O stretching of CO on this site is 2064 cm^{-1}, very close to the experimental observations of 2086 to 2090 cm^{-1}. We, therefore, conclude that the second ATR-FTIR peak appearing in EP-Cu attributes to the linear-adsorbed CO on the Cu^+ site, which plays an important role in C–C coupling as we demonstrated in our previous work: Cu^+ interacts weakly with CO, providing a suitable CO binding for CO coupling, which is beneficial for CO coupling to form C_2 products when combines with another strong CO binding site [46]. This also well explains the experimentally observed high selectivity of C_2H_4 on EP-Cu.

4. Conclusion

In summary, under identical reduction conditions, a high CH_4 selectivity was achieved on MP-Cu consist of a low-coordination Cu^0 phase, and a high C_2H_4 selectivity was realized using EP-Cu containing abundant Cu^0/Cu^+ sites. The CO adsorption studies showed that the strongly adsorbed CO_B on the low-coordination Cu^0 sites was apt to be hydrogenated to produce CH_4, and the co-existence of CO_B on the Cu^0 site and CO_L on the Cu^+ site were apt to be coupled to produce C_2H_4 (Fig. 4e). The DFT results were highly consistent with experimental results to further verify our conclusions. Our results expose the crucial factors that cause variation in reduction pathways for hydrocarbon productions and may guide future design of catalysts for both CO_2 and CO reductions.

Conflict of interest

The authors declare that they have no conflict of interest.

Acknowledgments

This work was supported by the National Natural Science Foundation of China (21875042), Shanghai Science and Technology Committee (18QA1400800), the Program of Eastern Scholar at Shanghai Institutions and Yanchang Petroleum Group. This work has benefited from the 1W1B beamlines at Beijing Synchrotron Radiation Facility (BSRF). The STEM study in this work is supported by the Frontier Research Center for Materials Structure, School of Materials Science and Engineering of Shanghai Jiao Tong University. The authors thank X.R. Zhao for assistance in TEM measurements.

Author contributions

Huisheng Peng and Bo Zhang supervised the project. Haipeng Bai, Shangyu Li and Zhenyu Zhou carried out all the experiments, characterization and CO_2 reduction measurements. Tao Cheng guided the DFT part and Miao Xie carried out the detailed calculation. Yujin Ji and Youyong Li also discussed the DFT calculation part. Zhiyou Zhou and Shigang Sun carried out CO adsorption studies. All authors discussed the results and assisted for the manuscript preparation.

Appendix A. Supplementary materials

Supplementary materials to this article can be found online at https://doi.org/10.1016/j.scib.2020.06.023.

References

[1] Shen H, Gu ZX, Zheng GF, et al. Pushing the activity of CO_2 electroreduction by system engineering. Sci Bull 2019;64:1805–16.
[2] Yang DR, Liu L, Zhang Q, et al. Importance of Au nanostructures in CO_2 electrochemical reduction reaction. Sci Bull 2020;65:796–802.
[3] Kas R, Kortlever R, Milbrat A, et al. Electrochemical CO_2 reduction on Cu_2O-derived copper nanoparticles: controlling the catalytic selectivity of hydrocarbons. Phys Chem Chem Phys 2014;16:12194–201.
[4] Liu GJ, Bai HP, Zhang B, et al. Role of organic components in electrocatalysis for renewable energy storage. Chemistry 2018;24:18271–92.
[5] Zhuang TT, Liang ZQ, Seifitokaldani A, et al. Steering post-C-C coupling selectivity enables high efficiency electroreduction of carbon dioxide to multi-carbon alcohols. Nat Catal 2018;1:421–8.
[6] He SS, Ni FL, Ji YJ, et al. The *p*-orbital delocalization of main-group metals to boost CO_2 electroreduction. Angew Chem Int Ed 2018;130:16346–51.
[7] Zhang B, Zheng XL, Voznyy O, et al. Homogeneously dispersed multimetal oxygen-evolving catalysts. Science 2016;352:333–7.
[8] Zhu MH, Tian PF, Li JY, et al. Structure-tunable copper-indium catalysts for highly selective CO_2 electroreduction to CO or HCOOH. ChemSusChem 2019;12:3955–9.
[9] Liu M, Pang YJ, Zhang B, et al. Enhanced electrocatalytic CO_2 reduction via field-induced reagent concentration. Nature 2016;537:382–6.
[10] Kortlever R, Peters I, Koper S, et al. Electrochemical CO_2 reduction to formic acid at low overpotential and with high faradaic efficiency on carbon-supported bimetallic Pd-Pt nanoparticles. ACS Catal 2015;5:3916–23.
[11] Back S, Yeom MS, Jung Y. Active sites of Au and Ag nanoparticle catalysts for CO_2 electroreduction to CO. ACS Catal 2015;5:5089–96.
[12] Qiao J, Liu YY, Hong F, et al. A review of catalysts for the electroreduction of carbon dioxide to produce low-carbon fuels. Chem Soc Rev 2014;43:631–75.
[13] Birdja YY, Pérez Gallent E, Figueiredo MC, et al. Advances and challenges in understanding the electrocatalytic conversion of carbon dioxide to fuels. Nat Energy 2019;4:732–45.
[14] Kortlever R, Shen J, Schouten KJ, et al. Catalysts and reaction pathways for the electrochemical reduction of carbon dioxide. J Phys Chem Lett 2015;6:4073–82.
[15] Ma XF, Li Z, Achenie LE, et al. Machine-learning-augmented chemisorption model for CO_2 electroreduction catalyst screening. J Phys Chem Lett 2015;6:3528–33.
[16] Eilert A, Cavalca F, Roberts FS, et al. Subsurface oxygen in oxide-derived copper electrocatalysts for carbon dioxide reduction. J Phys Chem Lett 2017;8:285–90.
[17] Montoya JH, Peterson AA, Nørskov JK. Insights into C–C coupling in CO_2 electroreduction on copper electrodes. ChemCatChem 2013;5:737–42.
[18] Peterson AA, Nørskov JK. Activity descriptors for CO_2 electroreduction to methane on transition-metal catalysts. J Phys Chem Lett 2012;3:251–8.
[19] Lee CW, Shin S, Jung H, et al. Metal-oxide interfaces for selective electrochemical C–C coupling reactions. ACS Energy Lett 2019;4:2241–8.
[20] Zhou YS, Che FL, Liu M, et al. Dopant-induced electron localization drives CO_2 reduction to C_2 hydrocarbons. Nat Chem 2018;10:974–80.
[21] Reske R, Mistry H, Behafarid F, et al. Particle size effects in the catalytic electroreduction of CO_2 on Cu nanoparticles. J Am Chem Soc 2014;136:6978–86.
[22] Feng XF, Jiang K, Fan S, et al. A direct grain-boundary-activity correlation for CO electroreduction on Cu nanoparticles. ACS Cent Sci 2016;2:169–74.
[23] Sheng T, Sun SG. Identifying the significance of proton-electron transfer in CH_4 production on Cu (100) in CO_2 electro-reduction. J Electroanal Chem 2017;793:184–7.
[24] Weng Z, Jiang JB, Wu YS, et al. Electrochemical CO_2 reduction to hydrocarbons on a heterogeneous molecular Cu catalyst in aqueous solution. J Am Chem Soc 2016;138:8076–9.
[25] Zhong H, Fujii K, Nakano Y, et al. Effect of CO_2 bubbling into aqueous solutions used for electrochemical reduction of CO_2 for energy conversion and storage. J Phys Chem C 2015;119:55–61.
[26] Varela AS, Kroschel M, Reier T, et al. Controlling the selectivity of CO_2 electroreduction on copper: the effect of the electrolyte concentration and the importance of the local pH. Catal Today 2016;260:8–13.
[27] Sen S, Liu D, Palmore GTR. Electrochemical reduction of CO_2 at copper nanofoams. ACS Catal 2014;4:3091–5.
[28] Manthiram K, Beberwyck BJ, Alivisatos AP. Enhanced electrochemical methanation of carbon dioxide with a dispersible nanoscale copper catalyst. J Am Chem Soc 2014;136:13319–25.
[29] Mistry H, Varela AS, Bonifacio CS, et al. Highly selective plasma-activated copper catalysts for carbon dioxide reduction to ethylene. Nat Commun 2016;7:12123.
[30] Hori Y, Takahashi I, Koga O, et al. Selective formation of C_2 compounds from electrochemical reduction of CO_2 at a series of copper single crystal electrodes. J Phys Chem B 2002;106:15–7.
[31] Choon HB, Fan WY. Shape evolution of Cu_2O nanostructures via kinetic and thermodynamic controlled growth. J Phys Chem B 2006;110:20801–7.
[32] Gao DF, Scholten F, Cuenya BR. Improved CO_2 electroreduction performance on plasma-activated Cu catalysts via electrolyte design: halide effect. ACS Catal 2017;7:5112–20.
[33] Phil DL, Rafael QB, Thang DC, et al. Catalyst electro-redeposition controls morphology and oxidation state for selective carbon dioxide reduction. Nat Catal 2018;1:103–10.
[34] Kau LS, Solomon DJS, Hahn JEP, et al. X-ray absorption edge determination of the oxidation state and coordination number of copper: application to the type 3 site in rhus vernicifera laccase and its reaction with oxygen. J Am Chem Soc 1987;109:6433–42.
[35] Martens G, Rabe P, Schwentner N, et al. Improved extended-x-ray-absorption fine-structure (EXAFS) studies applied to the investigation of Cu-O, Cu-N, and Cu-Br bond lengths. Phys Rev B 1978;17:1481–8.
[36] Clark EL, Resasco J, Landers A, et al. Standards and protocols for data acquisition and reporting for studies of the electrochemical reduction of carbon dioxide. ACS Catal 2018;8:6560–70.
[37] Arena F, Italiano G, Barbera K, et al. Solid-state interactions, adsorption sites and functionality of Cu-ZnO/ZrO_2 catalysts in the CO_2 hydrogenation to CH_3OH. Appl Cata A 2008;350:16–23.
[38] Hadjiivanov KI. IR study of CO adsorption on Cu-ZSM-5 and CuO/SiO_2 catalysts: σ and π components of the Cu^+-CO bond. J Chem Soc Faraday Trans 1996;92:113–8.

[39] Khazaee M, Xia W, Lackner G, et al. Dispersibility of vapor phase oxygen and nitrogen functionalized multi-walled carbon nanotubes in various organic solvents. Sci Rep 2016;6:26208.
[40] Feng X, Dong CJ, Dan P, et al. Zr-Modified SBA-15 supported Ni catalysts with excellent catalytic performance of CO selective methanation in H_2-rich fuels. Catal Lett 2018;148:2967–73.
[41] Niu X, Zhao T, Yuan F, et al. Preparation of hollow CuO@SiO_2 spheres and its catalytic performances for the NO+CO and CO oxidation. Sci Rep 2015;5:9153.
[42] Zhu SQ, Li TH, Cai WB, et al. CO_2 electrochemical reduction as probed through infrared spectroscopy. ACS Energy Lett 2019;4:682–9.
[43] Satsuma A, Tojo T, Okuda K, et al. Effect of preparation method of Co-promoted Pd/alumina for methane combustion. Catal Today 2015;242:308–14.
[44] Choi C, Cheng T, Flores EM, et al. A highly active star decahedron Cu nanocatalyst for hydrocarbon production at low overpotentials. Adv Mater 2018;31:1805405.
[45] Xiao H, Goddard WA, Cheng T, et al. Cu metal embedded in oxidized matrix catalyst to promote CO_2 activation and CO dimerization for electrochemical reduction of CO_2. Proc Natl Acad Sci USA 2017;114:6685–8.
[46] Cheng T, Xiao H, Goddard WA. Nature of the active sites for CO reduction on copper nanoparticles: suggestions for optimizing performance. J Am Chem Soc 2017;139:11642–5.

Haipeng Bai obtained his B.S. degree in Environmental Science and M.S. degree in Materials Engineering at School of Natural and Applied Science, Northwestern Polytechnical University. Currently he is studying as a Ph.D. candidate majoring in Polymer Physics and Chemistry in the group of Prof. Huisheng Peng at Fudan University. His research interest focuses on the electrocatalysts.

Bo Zhang is currently a Professor at the Department of Macromolecular Science, Fudan University. He received his B.E. degree in Optical Information Science and Technology at Northwestern Polytechnical University (China) in 2006, and Ph.D. degree in Chemical Engineering and Technology at East China University of Science & Technology in 2011. He started as a Lecturer at the East China University of Science & Technology in 2011 and then worked at University of Toronto as a visiting scientist from 2015 before joining Fudan University in 2017. His research centers on electrocatalysts.

Huisheng Peng is currently a Professor at the Department of Macromolecular Science and Laboratory of Advanced Materials, Fudan University. He received his B.E. degree in Polymer Materials at Donghua University in 1999, M.S. degree in Macromolecular Chemistry and Physics at Fudan University in 2003, and Ph.D. degree in Chemical Engineering at Tulane University (USA) in 2006. He then worked at Los Alamos National Laboratory before joining Fudan University in 2008. His research centers on smart fibers for energy and electronics.